Mapping axon diameters and conduction velocity in the rat brain – different methods tell different stories of the structure-function relationship

Skoven CS[a,b], Andersson M[a], Pizzolato M[c,a], Siebner HR[a,d,e] and Dyrby TB[a,c]

(a) Danish Research Centre for Magnetic Resonance,
Centre for Functional and Diagnostic Imaging and Research,
Copenhagen University Hospital Amager and Hvidovre, Copenhagen, Denmark

(b) Center for Functionally Integrative Neuroscience,
Aarhus University Hospital, Skejby, Denmark

(c) Department of Applied Mathematics and Computer Science,
Technical University of Denmark, Denmark

(d) Department of Neurology, Copenhagen University Hospital Bisbjerg and Fredriksberg,
Copenhagen, Denmark

(e) Department of Clinical Medicine, Faculty of Medical and Health Sciences,
University of Copenhagen, Denmark

Corresponding authors:

Christian Stald Skoven, cskoven@cskoven.com
Tim Bjørn Dyrby, timd@drcmr.dk

Danish Research Centre for Magnetic Resonance (DRCMR),
Centre for Functional and Diagnostic Imaging and Research,
Copenhagen University Hospital Amager and Hvidovre, Copenhagen, Denmark

1. Abstract
We investigated the structure-function relationship of axons projecting through the corpus callosum. We measured transcallosal conduction times using optogenetically evoked local field potentials (LFP) and estimated conduction length with tractography based on *ex vivo* diffusion magnetic resonance imaging (dMRI). Axon diameters were quantified using transmission electron microscopy (TEM) and dMRI. Comparing quantifications from TEM of dehydrated tissue with cryo-TEM, revealed axon diameter shrinkage in the former case. With correction for shrinkage, diameters from TEM showed better alignment with dMRI. The measured LFPs predicted axon diameters too small for quantitation by dMRI. Conversely, the large axons quantified by dMRI had conduction times too short to be quantified from LFPs. Hence, the two modalities had differing sensitivity profiles with respect to axon diameter. This emphasizes the need to combine suitable modalities to map the full spectrum of the structure-function relationship, in consideration of a given modality's domain of sensitivity.

2. Introduction

The structure and function of neurons are intimately related at all levels of the nervous system. A prominent example of this rule is the tight positive association between the diameter of myelinated axons and the velocity of action potential propagation along the axon [1]. In the mid-20th century, Rushton et al. [2] put forward a formal theory to describe the relation between axon diameter, the amount of myelination, and conduction velocity; This proposed structure-function relationship was later studied extensively in many types of myelinated axons of the peripheral and central nervous system across different species [1–4]. The axonal size can be expressed in terms of the inner diameter of the axon proper, or as the outer diameter, including the myelin sheaths that wrap around the axon. The ratio between the inner and outer axon diameters of a given axon, referred to as "g-ratio", is relatively constant in the central nervous system, ranging between 0.7-0.8 across different animal species, [5–9]. Assuming that axons have a cylindrical shape, and an invariant g-ratio, the conduction velocity is directly proportional to fiber diameter, as is supported by both experiments [1] and simulation experiments [9]. The relative invariance of the g-ratio also implies that it is sufficient to measure the inner or outer axon diameter to infer the conduction velocity of an axon [10]. Notably, other physiological factors, such as the density of sodium channels within the nodes of Ranvier and the distance between the nodes [1,2,11], also impact conduction velocity [11,12]. Yet, it is the axon diameter that carries the most weight in determining conduction velocity [12].

The relation between axon diameter and conduction velocity has been studied extensively in peripheral nerves, but (for technical reasons) to a lesser extent in the brain's white matter [1,3]. The distribution of axon diameters varies among brain white matter tracts and depends on which brain regions are connected by the tract [7], as seen in the corpus callosum (CC), which contains most of the inter-hemispheric fibers of most mammalian species [13–15]. Light microscopy (LM) and electron microscopy (EM) of the CC have consistently shown that the axon diameter distributions vary across the midsagittal plane in mammalian brain [16–19]. The largest diameter axons are typically found in the interhemispheric connections between motor and somatosensory areas and between primary visual areas [16,19]. Caminiti and colleagues mapped the conduction velocities along different transcallosal connections in the monkey brain, based on axon diameter distributions from tracer-labelled axons [17,19]. By measuring the tract length from injected neuronal tracers or diffusion magnetic resonance imaging (dMRI) based tractography, they predicted conduction latencies between inter-connected regions from the conduction velocity estimates [19,20]. Their study showed good agreement between the predicted transcallosal latencies and those obtained with electrophysiological recordings - and likewise stimulation experiments in other animal studies [20,21].

In humans, the conduction time of the transcallosal pathway can be measured between the hand areas of the bilateral motor cortices (M1) using non-invasive brain stimulation techniques such as dual-site Transcranial Magnetic Stimulation (TMS) [22–25]. Conveniently, the indirect effect of engaging the callosal fibers is measurable non-invasively in the hand muscles by electromyography. However, such functional recordings have not yet been directly related to structural measurements of the responsible axons, although one study alluded to the distribution of diameters of the engaged axons [26].

In vivo, it is possible to obtain an estimate of axon diameter with dMRI, which exploits the restricted diffusion of water molecules to probe non-invasively the geometry of axons [27,28]. The diameter estimation relies on fitting a biophysical model to the measured dMRI signal, under the assumption that axons are cylindrical [27,29]. Using the AxCaliber model, Horowitz et al. estimated the axon diameter distribution in living humans and correlated the mean diameter index with conduction velocities obtained from electroencephalography (EEG) during perfor-

mance of behavioral tasks and exposure to visual stimuli [30]. However, the dMRI-based diameters exceded the values expected from histology [27–29]. Moreover, recent 3D EM and X-ray nanoholotomography (XNH) studies in rodent [31,32] and primate [33] brains demonstrate that real axons exhibit variations of diameter and direction (micro-dispersion or tortuosity) along their trajectory. Hence, single-caliber, cylindrical axons are a fiction, and the biophysical models used to estimate diameter may thus give biased results when not accounting for real axonal morphologies [33,34]. While advances in dMRI technology have enabled mapping of the microstructure of white-matter pathways *in vivo*, it remains a challenge to derive the distribution of axon diameters in a specific tract from dMRI experiments and to relate these diameter estimates with the conduction velocities of that white matter tract. The overestimation of diameter from dMRI due to axonal micro-dispersion can be circumvented with powder averaging techniques, as shown in animals and humans [34–37]. However, as with conventional dMRI diameter estimation approaches, powder averaging is subject to an inherently limited range of sensitivity to axon diameter [34,36]. This range depends on the MRI hardware and imaging protocol, e.g., gradient strength [38,39] and signal-to-noise ratio (SNR) [34,40], and gives an upper and lower bound of measurable axon diameters. The dMRI signal for axons of diameter exceeding the upper bound can be attenuated into the noise floor [34], while axons with diameters below the lower bound will appear stick-like, with zero diameter [27,36,41–43]. Contrary to a simple arithmetic mean of the diameter distribution, the diameter estimate from dMRI is weighted towards large diameters, due to the nature of the scaling of signal attenuation, as well as the larger volume of such axons [27,36,41–43]. Comparisons of estimated axonal diameter between dMRI and histology thus require calculation of a weighted mean diameter from the observed histology-derived diameter distributions. Additionally, the impact of tissue shrinkage on axon diameter estimation in resin-embedded tissue samples for EM imaging is apt to cause discrepancies between what is measured and the actual *in vivo* diameter [28]. There are reports of white matter shrinkage factors between 0% and 65% caused by tissue sample preparation [16,28]. In cortical grey matter, a comparison of cryo-fixation, which leads to minimal shrinkage, with classical aldehyde fixation, dehydration, and resin embedding showed a 31% shrinkage of total volume by the latter method [44]. How tissue shrinkage specifically affects axon diameter is still an open question.

This study aims to explore the structure-function relationship, described by Hursh [1] and others [10] , of CNS axons with measurements of structure and function from the same animals. Our approach stands in contrast with the more common approach of correlating functional or structural measures to their counterparts from other studies. Specifically, we aimed to compare invasive and non-invasive structural imaging modalities to measure the axon and myelin diameters, and to determine their structure-function correlates with electrophysiological recordings. We targeted the well-described CC interhemispheric cortico-cortical projection between the primary motor cortices (M1) in rats. As a functional readout, we recorded the evoked response as local field potentials (LFP) after optogenetic stimulation of excitatory neurons in the M1 region of the contralateral hemisphere [45]. The pathway lengths were obtained through tractography from dMRI scans of the *post mortem* brains. These pathway lengths served to transform the measured latencies of the interhemispheric connection between the bilateral motor cortices into conduction velocities, and thereby to predict the corresponding axon diameters. We next used TEM and dMRI to map the axon diameter distributions and g-ratios in the midsagittal region of the CC. Thus, we based the predicted conduction latencies on the measured axon diameter distributions, g-ratio, and pathway length. Finally, by comparing cryo-fixation to classical aldehyde fixation, dehydration, and resin embedding, we explored how tissue preparation methods affected the estimation of axon diameters.

3. Results

3.1 Recording the Transcallosal Conduction Time

The latencies from three transcallosal evoked responses i.e., the P1 peak, N1 onset, and N1 peak latencies, as outlined in Fig. 1a, were recorded in 16 animals (Supplementary Table 1). We obtained the recordings under stimulation conditions that produced a reliable N1 peak, which typically included higher stimulation intensity (≥ 1 mW) and/or longer stimulation durations (≥ 1 ms). The mean latency ± mean of *within*-animal standard deviation (± SD) was 5.6 ± 0.3 ms for P1 (N=13), 7.2 ± 0.3 ms for the N1 onset (N=14) and 11.8 ± 0.5 ms for the N1 peak (N=14), respectively, as shown in Fig. 1b. The P1 peak was the earliest transcallosal response that was consistently detectable across most animals (N=13), and was thus used as an indicator of the transcallosal conduction time (TCT). In comparison to the *within*-animal SD of the latencies, the *between*-animal SDs were relatively large, being 1.49, 1.81, and 1.84 ms for the P1 peak, N1 onset, and N1 peak, respectively. In other words, there was more variability in latencies recorded from different animals, as opposed to latencies from repeated experiments, despite our systematic use of 42 different combinations of stimulation parameters within individual animals. This indicates that the obtained latencies were more robust within animals than between animals. As the variation between animals might reflect differing electrode depths, we also measured the electrode depths on high-resolution structural T2-weighted MR images in five animals. The mean (± SD) depth of 1045.23 ± 47.55 µm (N=5; Supplementary Table 2) suggests that depth variation was negligible.

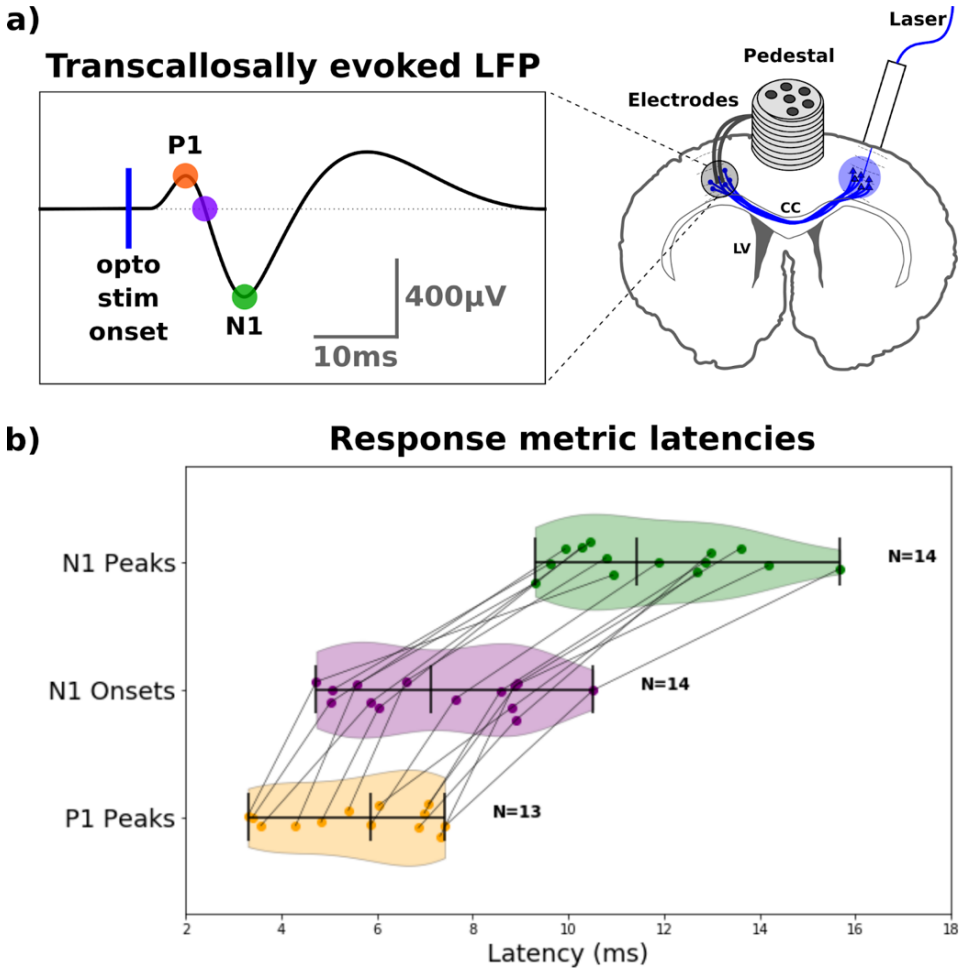

Figure 1: Conduction latencies obtained through optogenetic stimulation and electrophysiology, measured as local field potentials (LFP). a) Optogenetic stimulation of the right M1 and electrophysiological recording in the left M1. Orange dot: P1

peak; Purple dot: N1 onset; Green dot: N1 peak. **b)** Plot of median values of peak detections for all animals [45] in reliable conditions, with coefficient of variation for the N1 peak being < 1.00. Colors correspond to the insert in subfigure (a). The group means are depicted as the middle vertical line in each of the three metrics, and the outer-most vertical lines represent the minimum and maximum values for each metric.

3.2 Mapping the pathway length to estimate the conduction velocity

The viral injection in the right M1 targeted excitatory neurons (through the CamKIIα promoter) projecting through the CC to the contralateral M1 (Fig. 2a). Since these optogenetically stimulated neurons (Fig. 1) were also conveniently fluorescence-labeled (Fig. 2b), we were able to detect the projections through the mid-body of the CC with fluorescence light microscopy. The expression of enhanced yellow fluorescent protein (EYFP) was present in the superior half of the anterior midbody of CC (Fig. 2b, magnified in the red box insert).
Fig. 2c illustrates that tractography in the same animal was able to reconstruct the interhemispheric connection between the stimulation (right M1) and the recording sites (left M1). Indeed, a visual inspection of Fig. 2c confirmed that the tractography overlapped with the CC projection region from histology – and informed the subsequent histological sampling of the relevant region for EM quantitation of axon diameter. The connection length across all animals was 11.47 ± 0.47 mm (mean ± SEM; N=8; Supplementary Table 3). We present individual pathway lengths, as well as the variation between animals, in Supplementary Table 3.

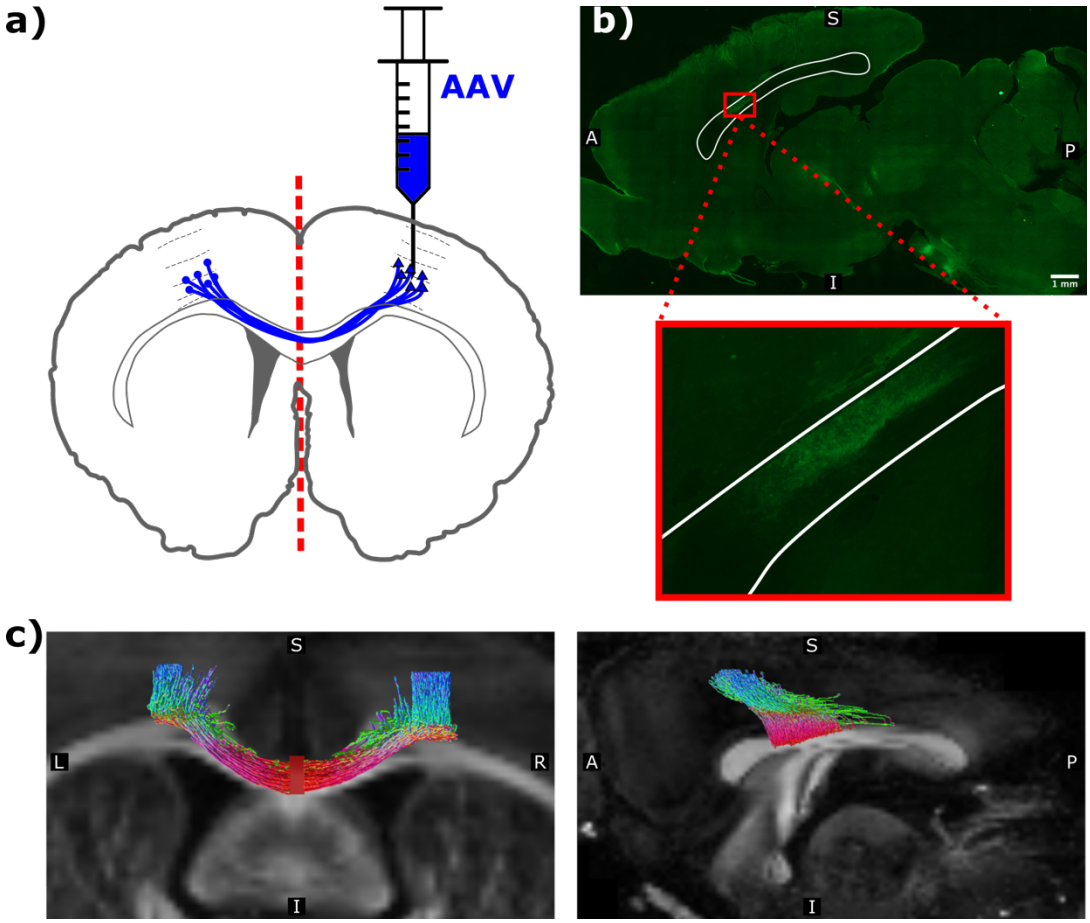

Figure 2: Viral expression and mapped motor pathway of the corpus callosum of rat14.5. a) Illustration of the viral injection in the right M1**. b)** Digitally stitched mid-sagittal image composed of multiple 10x magnification images acquired by fluorescence microscopy traversing the whole slice. Green corresponds to the expression of enhanced yellow fluorescent protein (EYFP) from the virally transfected neurons, highlighting the projection pathway between the primary motor cortices through the CC. The insert figure is an enlarged view of the small red box in the top panel. White lines delineate the contour of the mid-sagittal CC. Scale bar corresponds to 1 mm. **c)** Coronal (left panel) and sagittal (right panel) view of the dMRI scan (FA

map) of rat33.1, overlayed with the tractography streamlines projecting between the seeding region (located in the left M1 and right M1), projecting towards and terminating in the mid-sagittal region (filled red rectangle in the coronal section, left). The color-coding of tractography streamlines indicates their local direction, with red being left/right, green being anterior/posterior, and blue being superior/inferior.

3.3 Measuring the axon diameters and g-ratios

To predict conduction velocities from structural measurements, using equation (2) in Methods, we obtained estimates of axon diameters from both *post mortem* dMRI and subsequently axon diameter and g-ratio measures from Epon-TEM images from the same brain, in a subgroup of the animals (N=4 out of N=7 and N=5, for dMRI and Epon-TEM, respectively). We prepared an Epon-embedded sample from the midsagittal CC, where fluorescently labeled axons projected through (Fig. 2b) for TEM examination (Fig. 3a and 3b). Axon diameters and g-ratios were segmented automatically using AxonDeepSeg [46].

Figures 3c and 3d show the axon segmentation results from a representative case among 79 TEM images from rat14.1, and the corresponding histogram of the axon diameter distribution (N = 853 axons). The gamma distribution of the axon diameter distribution has a mode of 0.48 µm (mean = 0.52 µm; var = 0.02; skew = 0.57), with few axons being larger than 1.0 µm. Notably, the axon diameter distribution associated with the Epon-TEM methodology tended to have a slightly visible shoulder (or "second mode") of 0.66 µm (Fig. 3d, dash-dotted line). This apparent second mode indicates a possible bimodal distribution of the myelinated axons within the CC, corresponding to small and larger diameter sub-populations.

To explore if the classic tissue preparation approach of aldehyde fixation, dehydration, and resin (Epon) embedding affected the shape of the axon diameter distribution by shrinkage, we performed cryo-fixation and -embedding of tissue from another similar animal (rat4.2). Due to the specific requirements for sample preparation for cryo-TEM, neither dMRI nor Epon-TEM were acquired for this subject. In the same CC region as for Epon-TEM, we manually segmented axons (N=603) from the 15 collected cryo-TEM images, as shown in Fig. 3e. The fitted gamma distribution (a = 4.341, b = 0.194) had a mode of 0.64 µm (mean = 0.84 µm; var = 0.16; skew = 0.96), which is one third higher than the mode for the Epon-TEM. Compared with Epon-TEM, the tail of the distribution was wider, having a skewness of 0.96 compared with 0.57 for the representative Epon-TEM image. The Cryo-TEM histogram also showed a "shoulder" in the axon diameter distribution at 1.25 µm (Fig. 3d, dash-dotted line). This shoulder were more clearly separated from the primary mode in comparison to Epon-TEM (Fig. 3d vs. 3f).

Finally, using dMRI we estimated the diameter along the bilateral M1 projection within individual ROIs delineated by tractography (Fig. 2c), this being within the same animals used for mapping conduction latency with optogenetically evoked LFPs and axon diameter quantification by Epon-TEM. Figure 3g shows axon diameter estimates in a midsagittal slice of the CC, and an outline of the tractography ROI where M1 projects through. Across the CC, as seen in Fig. 3g, as well as along the contralateral M1 tract, some voxels show axon diameters of zero. Excluding these voxels along the M1 projection, the distribution mode of this animal (rat14.1) was 1.34 ± 0.42 µm (mode ± SD). For the voxel distributions of all animals, see Supplementary Fig.3. Fig. 3h shows the simulated expected sensitivity profile of the experimental dMRI setup to axon diameter when accounting for the used acquisition parameters and SNR[34]. There were lower and upper diameter bounds of the linear sensitivity range around 2 and 5.5 µm, respectively. Below the lower bound, there was a broader transition area between 1 - 2 µm with large uncertainty in diameter estimations, i.e., on average, the estimated diameter was underestimated, approaching zero or a constant value for axons with diameters of approximately 1 µm

(Fig. 3h). Hence, MRI voxels in which the diameter is estimated to be zero could potentially correspond to real diameters of 2 µm or lower.

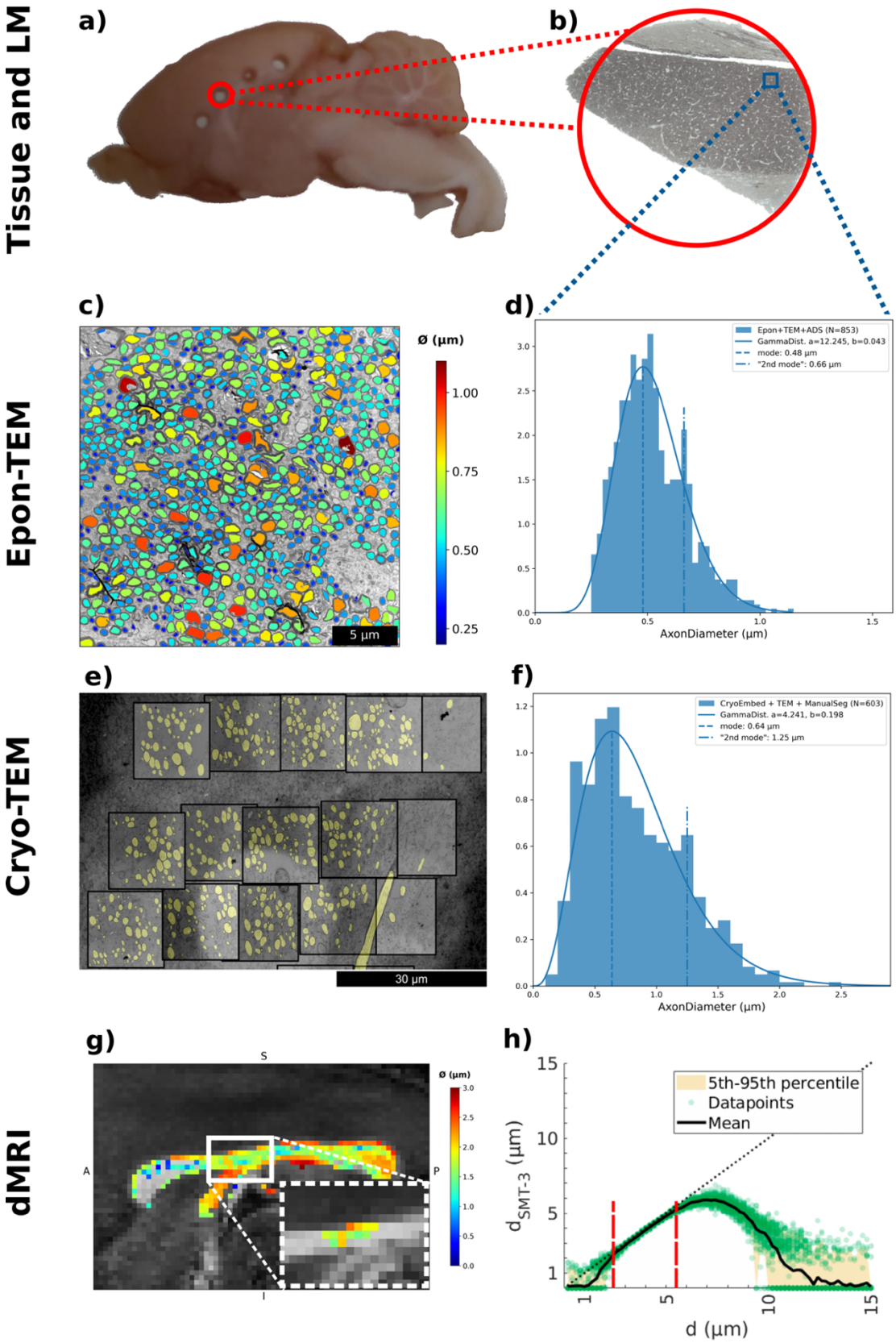

Figure 3 (previous page): Axon diameter measurements in corpus callosum using different imaging techniques. a) Mid-sagittal slab (~ 3 mm thick) with Ø = 1 mm punctures. **b)** Cross section of the EPON-embedded puncture, imaged with light

microscopy at 10x magnification. **c)** 4200x magnification sample window from rat14.1 (same as in panel g), roughly corresponding to the blue square insert in panel b. Segmentation of axons is colored according to their diameter (color bar to the right). **d)** Histogram of the distribution of axon diameters in CC automatically segmented and estimated with AxonDeepSeg of this particular TEM image in panel c, from the CC in the Epon-embedded and sectioned sample. **e)** Overview TEM image from Cryo-fixated and -embedded CC-tissue (Cryo-TEM) from a different animal (rat4.2). FOV: [75 x 75] µm, magnified to FOV: [19x19] µm (black box inserts) for quantification), **f)** Axon diameter distribution from TEM of the cryo-fixed and EPON-embedded CC tissue. **g)** dMRI axon diameter distribution from rat14.1 (same as in panel b) of whole CC.A = anterior, P = posterior, S = superior, I = inferior. The white box insert indicates the ROI voxels determined by tractography from the same rat. **h)** The sensitivity profile to the diameter of the dMRI acquisition for Rician noise with a signal-to-noise ratio of 50, showing the estimated cylinder diameter vs. the ground truth diameter, d.

3.4 Multi-modal structure-function correlation

Segmentations of Epon-TEM images were obtained in five of the 13 rats in which a P1 peak was detected, resulting in a group mean (± SD) of the distribution modes of 0.36 ± 0.04 µm (N=5; Supplementary Fig. 2). The axonal g-ratios were also estimated from the TEM segmented axons (Supplementary Fig. 1), which produced a group mean (± SD) of the g-ratio distribution medians of 0.68 ± 0.03 (N=5), this on close agreement with the typical literature value of 0.7. Axon diameter distributions as well as g-ratio distributions overlapped between animals (Supplementary Fig. 1 and 2). Similarly, the small shoulder in the axon diameter distribution (Fig. 3d) was evident in all animals (Supplementary Fig. 2).

The structure-function correlation between the measured structure (axon diameter distributions) and function (transcallosal conduction time, TCT), as well as their corresponding predicted counterparts, are shown in Fig 4. The conversion between the measured and the predicted TCTs and axon diameters used the group mean g-ratio (0.68 ± 0.03; N=5) and the group mean pathway length (11.47 mm ± 0.47, N=8) obtained from tractography (Fig. 2). Using the structure-function relationship (Eq. 1 and 2 in Methods), the group mean (± SD) of TCTs (5.57 ± 1.49 ms; N=13) obtained from functional measures of individual animals corresponded to the axons with mean (± SD) diameters of 0.28 ± 0.09 µm (N=13). Such diameters extended from below and up to the mode of the diameter distributions quantified with TEM.

The relative percentage shrinkages between Epon- and Cryo-TEM were 33% for the mode and 48% for the shoulder. This suggests that for Epon-TEM, the population of small axon diameters belonging to the mode of the axon diameter distribution shrinks less than the corresponding population of larger axons belonging to the second mode or shoulder of the distribution; larger axons shrink more.

To compensate for the shrinkage of axon diameters as part of tissue processing for Epon-TEM, we applied a fixed mean shrinkage factor of 40% to the axon diameter distributions (N=5), this being the average of the two modes, as noted above. The vertical dotted lines (Fig. 4, row 2) show that the mean of the shrinkage-corrected Epon-TEM axon distributions is close to that of the Cryo-TEM (Fig. 4, row 3; Supplementary fig. 3). The axon diameters predicted from the measured TCT overlaps with the small axons below and up to the mode of the diameter distributions from Epon-TEM and Cryo-TEM (Fig. 4, row 1 vs. rows 2 and 3).

The arithmetic mean voxel distribution of dMRI-estimated diameters shown in Fig. 4 (row 4) have no simple relation to TCT, due to the weighting of the dMRI diameter estimate towards larger diameters (Eq. 1 in Methods). As such, we estimated the weighted mean diameter from the shrinkage-corrected Epon-TEM (dash-dotted vertical lines, Fig. 4, row 2) and Cryo-TEM (dashed vertical lines, Fig. 4, row 3) axon distribution to be compared with dMRI. Figure 4 (rows 2 and 3) shows that the weighted mean axon diameter from Epon- and Cryo-TEM are

lower, despite being close to that obtained from dMRI. The smaller diameter axons, likely responsible for the measured TCT in Figure 4 (row 1), are not directly quantifiable with dMRI. The between-animal variation of the dMRI-estimated diameters is larger than the TEM results obtained on the same animals. This suggests that axon diameters detected by dMRI in some animals mostly fall within the non-linear transition region of the sensitivity profile (Fig. 3h), which likely accounts for the large between-animal variation.

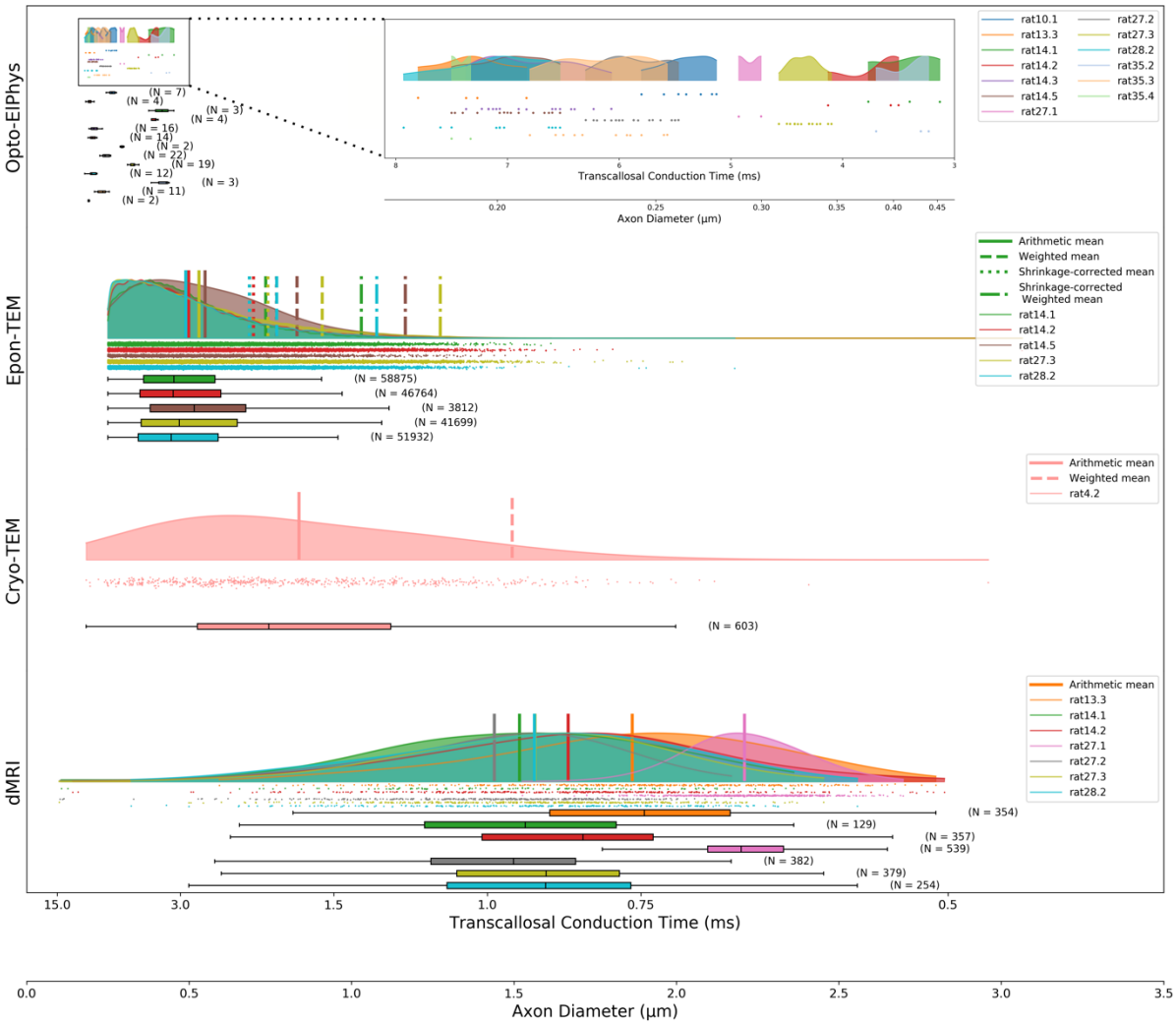

Figure 4: Structure-function relationships of measured and predicted values of all the modalities applied to the rat brain presented on a double x-axis, which represent latencies and diameters, respectively. Hence, individual points lying below the half-violin correspond to individually measured data points (denoted "N") of either the transcallosal conduction time in ms (Opto-ElPhys), or axon diameters in µm (Epon-TEM, Cryo-TEM, dMRI). Each distribution corresponds to data from one animal (depicted in different colors). For the axon diameter distributions (TEM and dMRI data), the arithmetic means are shown as solid vertical lines. For the TEM data, the weighted mean diameters (for comparison with dMRI) are shown as dashed vertical lines. For the Epon-TEM data, the mean of the shrinkage-corrected distribution as well as the weighted mean diameter are shown as dotted vertical lines and dash-dotted lines, respectively. The two x-axes depict the corresponding prediction of TCT, based on axon diameter, and vice versa - converted by a fixed g-ratio (g = 0.68; N = 5 rats) and the mean estimated projection pathway from tractography of all dMRI scanned animals (L = 11.47 ± 0.47 mm; N = 8 rats).

4. Discussion

Our main finding was that the TCT latency from LFP measurements in the intact rat brain corresponds to the small axonal subpopulation with diameters extending up to the mode of the diameter distribution as obtained with histology. Thus, we could not correlate the structure and

function relationship of the population of larger axons. We found large variations in the estimated axon diameter distributions across the different modalities, but since we used the same animals, we can attribute the variation in the main to the employed model and to tissue preparation procedures. Concerning the latter factor, we found differing shrinkages according to the diameter distributions between Epon-TEM and cryo-TEM approaches. The latter preserves better the *in vivo* tissue proportions, and is thus closer to the hydrated tissue state in our *ex vivo* dMRI measurements. Our finding suggests that larger axons shrink more than the smaller axons of diameter around the mode of the distribution (48% vs. 33% shrinkage). The means of shrinkage- and weighting corrected axon diameters of Epon-TEM did not fully agree with those from dMRI, whereas the weighted mean of the cryo-TEM data overlapped with the means from dMRI. This is as one might expect, since the latter approach only provides accurate and reliable estimates of diameter when the axons are within the detectable range, i.e., above the diameter lower bound. Hence, our findings suggest that one must consider the sensitivity profile of the measuring methodology for correct interpretation of the predicted Hursh-based[1] structure-function relationship.

4.1 Predicting axon diameters from the transcallosal conduction times

We used the peak of the first positive deflection of the transcallosal response, P1, as an indication of TCT. Our latency measurements of the P1 peak were stable on a sub-millisecond scale within animals (SD: ± 0.26 ms), despite having used different stimulation parameters [45]. However, the TCTs between animals, varied by several milliseconds (SD: ± 1.49). The large between-animal difference in TCT is not explicable by the small variations in the pathway length, as obtained from tractography [20,47,48]. Previous studies have estimated the length of the transcallosal pathway as a straight or curvilinear distance between the stimulation and recording position, which is a less precise approach than tractography [17,49]. The former approach would result in vast underestimation of the pathway, and thus predict a faster TCT. Notably, none of the previous studies collected axon diameters and TCT in the same animals so to confirm the structure-function relationship seen the present study.
The observed functional variation between animals might instead be explicable by differences in electrode depths. To record the evoked LFP response, we used relatively thick stereotrodes (with a fixed implantation position), achieving a standard deviation of the electrode depth of about ~50 µm, i.e., 5% of the intended depth of 1 mm in M1, as revealed with high-resolution *ex vivo* MRI. However, Iordanova and colleagues [50] demonstrated that the local voltage differences of the transcallosal evoked response in the S1-forelimb area are greatly affected by the cortical depth of the recording electrodes (cf. their Fig. 5d) [50]. This may hold true also for the area we investigated (M1), such that even slight differences in electrode depth could have perturbed the peak amplitudes and latencies of the P1 and N1. Saiki and colleagues also performed optogenetic stimulation of M1, acquiring multi-unit activity (MUA) measurements with a high temporal resolution in the contralateral M1 [66]. They found transcallosal responses from multiple individual neurons, with mean (± SD) latencies of 5.2 ± 1.8 ms, thus in general agreement with our LFP findings. Because of the higher density of smaller axons in the CC, one might expect that the MUA recordings in the cortex would correspond to these small-diameter axons, which could explain the agreement with our LFP results. However, a single-unit or MUA approach would likely allow us to record and focus on the spiking also governed by the larger axons, despite their lower density - an opportunity not possible with our LFP recordings.

Despite the between animal variations in TCT, our results agree with other studies. Hoffmeyer and colleagues [51] recorded the intracortical transcallosal responses as LFPs in the *sensory* area of rats after *electrical* stimulation in the contralateral homologous area. They reported a conduction delay as brief as 4 ms, and the latency to the first peak of 9 - 11 ms after stimulation.

They did not investigate the potential effects of different electrode depths, but rather used a fixed position between 300 - 400 µm, i.e., considerably closer to the cortical surface than our recordings. Seggie and Berry [52] also performed cortical *electrical* stimulation and LFP recordings of the interhemispheric response in rats, and found 8 ms latencies of the first peak [52]. They stimulated and recorded in an unnamed cortical area (±3 mm lateral to the bregma) with electrodes placed on the cortical surface. Although a more indirect way of measuring the transcallosal response, their method may have been spared confounds due to differing electrode depth between animals.

In humans, investigations of the TCT between the motor cortices using a dual-coil transcranial magnetic stimulation approach have given latencies of 5-13 ms [22,23,25], and 8-10 ms when stimulating the dorsal premotor cortex [24]. A similar dual-coil TMS approach, placed above the bilateral M1s, has been used to probe the latency distribution of callosal connections [26]. Specifically, they measured in that study the largest proportion of interhemispheric facilitation and inhibition, with 0.1 ms increments in the interstimulus interval. Their results indicated the largest proportions of fibers governing the facilitation at 3.8 ± 0.4 ms and inhibition at 9.0 ± 0.3 ms. Interestingly, their results give a hint that a distribution of differently sized axons governs the transcallosal response, even when using a non-invasive approach. This agrees with our structure-function relationship hypothesis that the P1 peak measured with LFP corresponds to an axonal subpopulation at the mode of the diameter distribution, as seen in our histological data. Such a population would likely produce a synchronized response with approximately the same latency.

Interestingly, the TCT measured with TMS in humans, as well as measures [21] and predictions [19,20] from monkeys, are comparable to those obtained in our rat study. The relatively constant TCT across species indicates structural and/or functional adaptations, since the interhemispheric pathway length obviously increases with brain size. Various studies indicate that the largest CC axons increase with brain size [17,49,53], at least to a certain degree, which predicts faster conduction velocity in those larger axons [17,49]. However, irrespective of brain size, the modal axon diameter is relatively constant across mammalian species [17,29,54]. Minor variations around this distribution mode cannot compensate for the increased conduction distances incurred by the 750-fold greater volume of human brain compared to the rodent brain [28,55,56]. Not even tissue shrinkage effects of 40% could explain the constancy of TCTs despite such differences in brain size. Using the TCTs estimated with TMS in humans (5-13 ms [22,23,25]) and an estimated interhemispheric pathway length (111.4mm[20]-122.4 mm[17] for the motor sector), and a g-ratio of 0.7, Eq. (1) and (2) (Methods), give predicted axon diameters in the range of 1.09 – 3.12 µm. This range corresponds to a population of axons exceeding the modal human axon diameter in the CC [17] and is in alignment with the expectation that TMS primarily activates the larger excitatory neurons [57,58]. In contrast, using the LFP-based recordings in rats, we found that TCT corresponds to the axons of diameter below the mode. Thus, scaling of axonal diameter seems unlikely to account for TCT constancy across species of differing brain size. However, our findings do support our hypothesis that the axon diameter distribution may contain different populations, with different latencies, which may in turn have different functional contributions. It is therefore essential to consider the specificity and sensitivity profile of an applied stimulation and electrophysiological recording technique (e.g., optogenetics and contralateral LFP recordings vs. TMS and peripheral EMG recordings) when attempting to elucidate indirectly the structure-function relationship of intrahemispheric axonal conduction. Similarly, from a structural point of view, when predicting conduction velocities from an axon diameter distribution, one cannot generalize to the mean or mode of the distribution (as is traditionally done), but must consider the possibility of subpopulations of differing axon diameters[33].

4.2 Measured axon diameter distributions depend on the tissue preparation

We observed variations in the measured axon diameter distributions depending on the tissue preparation method, which influences the prediction of conduction velocity. In the axon diameter distribution estimated from Epon-TEM images, we observed a weak "shoulder" after the primary mode – or, in other terms, a second mode. This is indicative of two axonal sub-populations with smaller and larger axon diameter distributions [33]. When using cryo-fixation, which should maintain a structure closer to an *in vivo* state, we also found two modes, but with better separation between the primary and secondary modes. Interestingly, when comparing the two tissue preparation techniques, the larger axons were more affected by shrinkage than were the smaller axons, i.e., 48% versus 33%. The non-linearly appearing shrinkage differences might bear some relation to conduction velocities. In particular, internal resistance for the sodium ions within the axon affects the velocity of their movement [59]; the larger the axon, the lower the electrical resistance [60], which likely reflects lesser interference from macromolecules of the cytoskeleton. Altogether, this suggests a higher water content in the large diameter axons, which renders them more vulnerable to shrinkage during the dehydration step used in the tissue preparation for Epon-TEM.

In white matter, tissue shrinkage factors from 0 to 65% have been reported during sample preparation [17,19,28,61] and used as a linear correction factor. However, realizing a true non-linear shrinkage correction would require measurement or modeling the shrinkage of individual axons in the complete distribution. Alternatively, two linear correction factors could be applied; one below and one above the mean diameter distanced between the two modes. Since the two modes in Epon-TEM could be challenging to localize accurately, we instead applied a single linear correction (Supplementary fig. 2), being the mean of the two shrinkage factors (40%). This mean shrinkage value is similar to the correction factor that used in previous studies [28]; its application to the Epon-TEM data gave a good correspondence with the Cryo-TEM data. This shrinkage approximation may be applicable for the axon distribution in the rat, where the distribution tail of the larger axons is small (Supplementary fig. 2), but might be unsuitable for the larger primate brain, where the distribution tail is more pronounced [17,20]. To determine the shrinkage factor in primates would likely require application of cryo-TEM – which could be explored in future studies. Since *ex vivo* MRI is obtained in hydrated tissue, applying an appropriate shrinkage factor is essential for comparing axon diameters with those obtained by Epon-TEM to avoid an underestimation of true axon diameters due to the tissue processing [27,28]. Grey matter is also affected by preparation-dependent shrinkage when compared to cryo-embedded tissue samples [44,62]. Similarly, synchrotron imaging of fixed hydrated cerebellum samples revealed the presence of larger cell bodies compared to dehydrated samples [62]. Altogether, our results suggest that a reliable shrinkage factor correction or the application of Cryo-fixation and -embedding can ensure accurate structure-function predictions with minimal dependence on the tissue processing procedure.

In this study, we observed overlapping axon diameter distributions obtained with TEM between animals. This is in accord with other studies (see Supplementary Table 4) showing similar distribution modes and ranges between individual animals and across species, when tissue preparation is performed in a consistent manner. In an investigation of different species, Olivares and colleagues [49] found the mode axon diameter to be 0.11 - 0.2 µm for smaller animals (e.g., rats) and large animals (e.g., cows and horses) [49]. However, other groups reported a larger modal axon diameter distribution in rats (≥ 0.8 µm) [29,36]. That the axon diameter distribution varies more between studies in a given species than for different species gives further indication that tissue preparation strategies can severely affect the results. Nevertheless, this consideration does not change our overall finding across animals that axons smaller and up to the mode of the axon diameter distribution generally agree well with the TCT (P1 peak) obtained from

LFP. However, comparing predictions of conduction velocity from structural data across studies calls for confirmation of conduction velocity in the same animal, as in this study.

4.3 The structure-function relationship with dMRI

We were unable to record latencies from LFPs, corresponding to axon diameters as large as estimated with dMRI with distribution modes of 1.3-2.2 µm. Given the structure-function relationship presented by Hursh [1] and others [5,10] and the estimated pathway length, the resulting TCTs would generally be ≤1 ms. This relationship is determined by individual axons with constant diameters along their lengths, and with axon diameters contributing with an equal weighting towards the distribution mean. The diameter estimates from dMRI are different, representing a weighted mean over the entire distribution of axon diameters, where larger axons have a greater contribution to the estimate [27,36,41–43]. Moreover, we found that the diameter estimation from dMRI has a sensitivity profile [38] giving non-zero diameter estimates when axon diameter is within or above the transition area (Fig. 3h). Below this range, the diameter estimation often fails, dropping to zero or a constant value [34,38]. Some voxels from our MRI estimates returned diameters of zero, suggesting that the weighted diameter distribution present in the tissue may have been within or below the transition area, i.e., below 2 µm. This complicates the structure-function correlation of dMRI diameter estimates with conduction times from the LFP method, which is unfit to detect large, fast-conducting axons; the two methods are sensitive and accurate within different diameter ranges.
Although some of the dMRI axon diameter estimates overlapped with the shrinkage-corrected and weighted Epon-TEM means, the weighted mean axon diameter from Cryo-TEM still agreed better with the dMRI estimates. We attribute this difference to the imperfect shrinkage correction we applied to the Epon-TEM axon diameters. Interestingly, dMRI showed a wide diameter distribution within animals, as also seen for Epon-TEM. Likely due to the sparser measurements in dMRI (less than 600 voxel estimates per animal) compared with Epon-TEM (~4000 - 59'000 axons quantified per animal), and the influence of the transition area, the between-animals variation is larger for the former method. Some variation in the dMRI diameter estimates for rescans and across primate subjects is however expected [35,38]. Nevertheless, even when comparing with shrinkage-corrected Epon-TEM diameters, we did not detect many axons of diameter exceeding the lower bound. We covered a large field of view (~10,000 μm^2 for N=1; 42,000-47,000 μm^2 for N=4) with Epon-TEM at 4200x magnification, thereby including most of the CC contained in the 1 mm puncture sample (see Supplemental Figure 4). This was done to also capture the sparsely distributed large axons in the CC to accommodate a methodological consideration mentioned in previous studies, namely a potential bias towards the densely packed smaller axons [33,36,63]. Further, we have recently shown that the mean diameter acquired from a 2D slice matches the mean 3D diameter along the trajectory of individual axons [33]. Therefore, even though we captured the axon diameters in an ultra-thin mid-sagittal 2D slice, this should also reflect axon diameters in 3D, as probed by dMRI.

In dMRI, the diameter lower limit is set by the gradient strength, acquisition parameters, SNR, and the model used to estimate diameters [35,38]. Veraart et al. used stronger gradients of 1500 mT/m versus our 600 mT/m and thereby reduced the diameter lower bound to about 1.6 µm [36]. In rats examined *ex vivo*, they reported a diameter of around 2.5 µm in the CC region of M1 projections. Given our acquisition setup, this agrees with our dMRI finding that the probed diameters are likely in the transition area of the diameter sensitivity profile (Fig. 3h). Additionally, the presence of axons with diameters in the transition area may explain the variation we observed in the dMRI results when compared with shrinkage-corrected Epon-TEM. Studies have presented *in vivo* axon diameter estimations in the human brain [27,35,36,64] with robust rescan findings [65]. Due to the hardware and SNR, those dMRI studies also had a diameter lower bound

on a scale of several micrometers [27,34]. Hence, the dMRI axon diameter estimates in humans should agree with TMS-based latencies, but not with latencies from the slower conducting smaller axons. Further, the fitting failed in some voxels of the rat brain, whereas whole brain axon maps are obtained for the human brain [35,36]. This discrepancy supports the existence of a population of much larger axons throughout white matter of the human brain, which are absent from the smaller rat brain.

4.4 Considerations

We used optogenetics to stimulate specifically the excitatory cortical projecting neurons. This is in contrast to electrical stimulation, where all neuron types in the vicinity of the electrode tip are affected [66]. Indeed, our histological investigation showed that the marker EYFP was profusely expressed in the CC projection area [45], confirming the preponderance of excitatory projection neurons. However, given that the callosal projecting cortical neurons are embedded in a matrix of excitatory pyramidal cells and inhibitory interneurons [67,68], some off-target neurons might also have been virally transfected. In this event the laser stimulus could have activated callosal projection neurons as well ipsilateral intracortical projections, with unpredictable effects on the transcallosal evoked response. This possibility might have been circumvented by a more specific approach such as Cre-dependent viral expression, targeting uniquely the callosal projection neurons. Even then, there might occur local or ipsilateral activation of inhibitory interneurons and/or excitatory pyramidal cells via bifurcating callosal projecting neurons.

Furthermore, the proportion of the segmented axons from TEM that were also optogenetically stimulated is unknown. Since only a very few axons in the CC are GABAergic [69], they would likely not have markedly affected the segmented axon diameter distribution. The different neurotransmitter components (glutamate and GABA) of the transcallosal evoked response have been investigated with pharmacological challenges during electrical [51,70] and also optogenetic stimulation [71,72]. Results of those studies indicated that the initial response (P1) is likely the excitatory postsynaptic potentials caused by the transcallosal glutamatergic response, whereas the subsequent peak (N1) might be inhibitory postsynaptic potentials from the local inhibitory GABAergic interneurons. However, our histological quantification of axon diameters performed on TEM images were uninformed by neuron type. Since glutamatergic neurons account for most of the callosal projections, it is reasonable to assume that most axons in our sampling areas were contributing to the LFP signal. Some of the segmented axons might however have been silent, and therefore spuriously included in the axon diameter distribution.

Although optogenetics is focally specific with respect to neuron type [67], and should not introduce a stimulation artifact, it has a potential caveat with respect to temporal delays in comparison to electrical stimulation. The temporal delay (t_{kON}) of hChR2-H134R is between 0.6 ms and 2.6 ms [68–70] depending on the stimulation intensity. As the latencies obtained from the optogenetic experiment arose from different laser stimulation intensities, adjusting for the onset latency would require individual adjustment values. Furthermore, with our experimental setup we could not measure the actual optogenetic stimulation delay, which would have required a patch-clamped approach with an additional electrode at the stimulation position. Applying a single fixed stimulation intensity would likely have given rise to even smaller differences in the obtained TCT. That said, we obtained sub-millisecond variation of latencies within animals, which suggests that the range of stimulation intensity had minimal differential effect on the latency. Taking into account the onset latency, the TCTs would likely have overlapped with a broader distribution of the axon diameters, including axons larger than the mode of the axon diameter distribution. This indicates that the prediction of axon diameters based on TCT should in the future should consider the temporal delay of the onset kinetics for optogenetic activation.

5. Methods

Electrophysiological data were collected in our previous study, where methods are described in detail [45]. All animal procedures were conducted in accordance with the ARRIVE guidelines, the European Communities Council Directive (2010/63/EU) and were approved by the Animal Experiments Inspectorate (2016-15-0201-00868) of Denmark.

5.1 Animals and surgery

16 young male Sprague-Dawley rats (NTac:SD-M; 4 weeks old) underwent stereotaxic surgeries (Stoelting Lab Standard, Digital Dual Manipulator; Wood Dale, IL, USA) [45]. In brief, we made craniotomies above the bilateral M1 (AP: +1.0 mm; ML: ±2.5 mm, relative to bregma), where the dura was punctured. In the right M1, we injected the viral inoculum (AAV5:: CamKIIα −hChR2(H134R)−EYFP; UNC Vector core) at a depth of -1.00 mm relative to the dura. A calibrated optic fiber implant (Ø = 55 µm) was later implanted at the same position. In the left M1, a stainless steel stereotrode pair (Ø = 127 µm) was implanted at the same depth to record the evoked potentials as LFP. The signal was amplified with gain factors of 100x - 1000x. In the former case, we multiplied the recorded signal by a factor of 10. Hardware filters were set to bandpass between 0.1 Hz and 50 kHz. The recorded LFP data was further filtered with a notch filter at 50 Hz and a 2nd order Butterworth band-pass filter between 3 Hz and 300 Hz. For further details, see the previous study [45].

5.2 Electrophysiological recording of optogenetically evoked transcallosal potentials

Four to seventeen weeks after surgery, the animals were exposed to a paradigm of blue laser light brain stimulation (λ = 447 nm) while recording the evoked responses as LFPs. Prior to the experiment, the animals had been anesthetized with dexmedetomidine and low dose isoflurane, as described in our previous study [45]. The available data from [45] included systematically varied stimulation durations and intensities (0.1-10.0 ms and 0.25-10 mW), resulting in a stimulation input parameter map of 42 different conditions. Each condition produced 150 individual trials, totaling 6300 stimuli per animal, with a few (< 8 trials per condition) being discarded for technical reasons. Trials were baseline-corrected using the mean value of the data points in the 10 ms period preceding the laser stimulation onset. The signal recorded from the two channels of the stereotrode was averaged for all trials for each individual condition. Data from one animal (rat33.1) were discarded due to lacking response after optogenetic stimulation, leaving 15 animals for peak detection and quantification.

Based on the data so obtained, we estimated the transcallosal conduction time (TCT), represented by the latencies of the first measurable transcallosal response. After visual inspection of the typical stimulation responses, we defined criteria for automatic peak detection for the first positive (P1) and negative (N1) deflections. Specifically, the time span for the two peaks was restricted to the ranges t = +1 ms to t = +9 ms for P1, and t = +5 ms to t = +20 ms for N1. The peaks were automatically detected using the following procedure: If the signal amplitude extended beyond the threshold of one standard deviation, based on the 100 ms epoc preceding the stimulus onset (from t = -105 ms to t = -5 ms), the maximum absolute amplitude of the deflection within the timespan was considered a peak. We manually inspected the results of automatic peak detection and and discarded erroneous cases. The peak onset of N1 was interpolated, as in the previous literature [73,74]. Specifically, we took the onset as the intersection of a first-order regression line on the peak slope, between 45% and 55% of the N1 peak minimum, and the baseline. For each condition, the signal amplitude of each individual trial was captured exactly at the obtained latency of the N1 peak to calculate the coefficient of variation (SD/Mean). This coefficient of variation served to determine the reliability of the peak within

each condition. Any conditions providing a coefficient of variation of the N1 peak below 1.00 were considered to be reliable. One animal (rat9.4; in addition to rat33.1, mentioned above) produced no reliable conditions based on this criterion, despite showing visible peaks in some conditions. Therefore, we obtained latencies from 14 animals.

The P1 peaks of the measured LFP signal were often insufficiently prominent to detect the P1 peak onset. Therefore, as an approximation of the TCT we instead used the median of the P1 peak latencies from all reliable conditions of each animal.

The data analysis was accomplished with custom-made python-scripts (https://git.drcmr.dk/cskoven/elphys), utilizing the open source analysis toolkit for Open-Ephys-data (https://github.com/open-ephys/analysis-tools).

5.3 Perfusion fixation

To extract the brains for further *post mortem* MRI and histological analysis, the rats were perfusion fixed immediately after the final optogenetic brain stimulation session. Here, anesthesia was induced with 5% isoflurane, followed by subcutaneous injection with mixture of Hypnorm® (Fentanylcitrat 0.315 mg/mL and Fluanisone 10 mg/mL; Department of Experimental Medicine, Panum, Copenhagen, DK), sterile water (Fresenius Kabi, Uppsala, Sweden) and Dormicum® (Midazolam 5 mg/mL; B. Braun, Germany) in a 1:2:1 ratio (3 mL/kg). Transcardial perfusion was initiated with 0.1 M potassium phosphate-buffered saline (KPBS) delivered at 15-20 mL/min for approximately 3 minutes, followed by 7-12 minutes of infusion with 4% formaldehyde (CellPath; Newtown, Powys, UK). The brain was extracted and post-fixed pin 4% formaldehyde at 4 ºC for at least 3 weeks. At least three weeks before MRI scanning the brains were placed in 0.1 M KPBS to remove free formaldehyde, thereby restoring T2 relaxation and thus increasing SNR in the subsequent MRI scans [28].

5.4 Post mortem MRI

5.4.1 Preparation prior to MRI scan

Before the histological process, a subgroup (N=8) of the *ex vivo* brains were MR scanned. The extracted intact brain was wrapped in a thin cloth sheet (Nonwoven swabs, Selefa; OneMed, Danderyd, Sweden), placed in a double plastic bag containing a minimal volume of KPBS, and allowed to reach room temperature prior to scanning. The brain was positioned on a mechanically stable sample holder custom-made with LEGO™ blocks to avoid introducing short-term instabilities into the acquired dw-MRI data set [56]. We used a cryo-coil setup, allowing for a 2.5-5x increase in SNR compared to regular room-temperature coils. The temperature at the surface of the non-cryo part of the cryo-coil was set to 24 degrees to ensure a constant temperature environment of the tissue during the scanning session. All MRI datasets were acquired on a 7T preclinical Bruker scanner (Bruker BioSpec 70/20 USR) using Paravision 6.0.1.

5.4.2 Diffusion MRI

For axon diameter estimation we used a three-shell pulsed gradient spin echo (PGSE) protocol with single-line readout. Three unique b-values with b = [24.450, 21.247, 17.560] s/mm^2, gradient strengths G = [590, 550, 500] mT/m, gradient separation (Δ) = 18 ms, and gradient duration (∂) = 8 ms were applied along 30 uniformly distributed diffusion gradient directions that were generated using the electrostatic repulsion method [75,76]. In addition, nine b=0 images were acquired. All shells used the same echo time (TE) of 28.5 ms and repetition time (TR) of 3500 ms and were acquired with an isotropic voxel size of 125 µm. Ten sagittal slices with no in-

between slice gap covered a limited field of view around the midsagittal region of the CC. Total acquisition time was 35 hours.

To assess the lower bound of measurable axon diameter, we calculated the sensitivity profile to axon diameter of this dMRI acquisition as previously described [34]. The signals from cylinders were analytically generated for diameters in the range 0.2 - 15.0 µm at 0.2 µm steps. Rician noise of a given signal-to-noise ratio (SNR) was added to the signals and the powder average cylinder model was fitted to obtain a diameter estimate. The Rician distributed noise was emulated by calculating the magnitude of complex Gaussian distributed noise in which the standard deviations of the real and imaginary components were both 1/SNR. The diameter estimation was performed 50 times for each diameter, with each repeat represented by a green data point in Fig. 3h. The sensitivity profile revealed a diameter lower bound of around 2 µm and an upper bound of around 6 µm for accurate estimation of the diameter.

For tractography, whole-brain dMRI data sets (isotropic voxel size of 125 µm; 80 axial slices; no slice gap; matrix: 128 x 128 x 80; FOV: 16mm x 16mm x 10 mm) were collected using a single shell with b-value of 4000 s/mm^2 (gradient strength (G) = 224 mT/m; Δ = 23 ms; ∂ = 7.5 ms) in 61 isotropic distributed non-collinear directions [77]. The scan was acquired with TE = 38.6 ms and TR = 3592 ms. Total acquisition time was 9 hours.

After acquisition, the dMRI data sets both for axon diameter estimation and tractography were denoised using the variance stabilizing transform and optimal shrinkage singular value manipulation method [78], and processed to remove Gibbs ringing artifacts [79] using the MRTrix3 software toolbox (RRID: SCR_006971).

5.4.3 High resolution structural image

A high-resolution structural 3D T2 weighted MR image was obtained for a subgroup of animals (N=5) to compare with histological slices, for determination of implant depths and for visualization. A "true" fast imaging with steady-state free precession (FISP) T2 weighted sequence acquired high-resolution whole-brain visualization with the following parameters: TR: 2.5 s; TE: 5.1 ms; matrix size: 256 × 256 × 128; field of view: 23.04 × 23.04 × 11.52 mm^3; Image resolution: 90 × 90 × 90 µm^3; Flip angle: 30 degrees, Averages: 40; and total acquisition time: 2 hours.

5.4.4 Tractography

To obtain an estimate of the length of the interhemispheric callosal M1 pathway, we performed probabilistic streamline tractography on the whole brain dMRI data set. To identify the position of injection sites, we used the high-resolution T2w-MRI scan. In combination with histological slices of the fluorescently labeled excitatory neurons, we confirmed the positions of the fiber and electrode implantations, as well as the axonal projection region through the midsagittal slice of the CC. The most robust way to segment the tract was proved to be summation of the length of two tractograms performed individually for each hemisphere. One tractogram emanated from the optical fiber depth and the other from the electrode depth, with both set to terminate in the midsagittal CC. All ROIs were drawn on fractional anisotropy (FA) maps generated in MRtrix3. The seed ROIs for each hemisphere were drawn axially just beneath the shaft lesion from fiber or electrode implantation. The target ROI was drawn covering the whole midsagittal plane of CC. Further, exclusion ROIs were drawn axially, just superior to the seed ROIs, thereby avoiding streamlines that erroneous projected into the shafts of either electrode or fiber implantations in the cortex. Finally, a set of exclusion ROIs were placed sagittally

(lateral to the implant regions) as well as coronally (anterior to the implant regions), and posterior to the CC projection area of. This was done to further exclude spurious streamline trajectories that obviously deviated from the main tract. Up to one million streamlines were seeded in the generation of each tractogram, with selection of a least one thousand streamlines. The mean (± SD) length of all streamlines were calculated. The tractography was based on constrained spherical deconvolution for fiber reconstruction, with performance of probabilistic tracking using the IFOD1 function with standard settings in the MRtrix3 toolbox [50]. In some cases, the tractography was unable to cover the full pathway into the gray matter at the fiber and/or electrode position. These path discrepancies, as well as the distance between the connecting tracts in the CC, were measured manually from the FA image. Tractography was performed on nine brains, where one was excluded due to unsuccessful tracking.

5.4.5 Axon diameter estimation from dMRI

The preprocessed multi-shell dMRI data sets for axon diameter estimation were normalized by the voxel-wise average of the b=0 images. The powder average for each b-value was calculated via the arithmetic average of the signals across the 30 diffusion encoding directions. The high b-values were such that the signal from the extra-axonal space could be approximated to be fully attenuated [36,80]. For the model fitting, as thus assumed that the signal only contained contributions from the intra-axonal space. An axonal signal model describing the spherical average of cylinders [33,35,81,82] was fitted to the powder average signals using the non-linear least squares approach in Andersson et al. [33]. That model assumed that the Gaussian phase approximation was valid.

The model fitted three unknown parameters of the following variables: the intrinsic diffusivity i.e., intra-axonal axial diffusivity (D_o), the intra-axonal perpendicular diffusivity ($D_\perp$), and the signal fraction of the intra-axonal space (v_a). The diameter could then be calculated from $D_\perp$ using the Van Gelderen et al. (1994) formulation for the PGSE signal perpendicular to a cylinder [83]. The intrinsic diffusivity was measured in individual brains from the principal direction within the CC region using the diffusion-tensor model fitted to the b-value of 4000 s/mm^2, and was kept constant for the fitting of axon diameter [27].

Finally, we estimated the axon diameter from dMRI in the bilateral M1 projection region of CC. A 3D ROI was placed in the projection region of CC, lying between the stimulation and recording area in the bilateral M1 areas, and automatically mapped by the streamlines from tractography. Axon diameters below 0.1 µm were discarded. The mean axon diameters from all voxels in the ROI were obtained and the mean (± SD) axon diameter was calculated for all animals.

5.5 Histology

After the *ex vivo* MR scanning, the brains were further processed for histological investigations. This entailed fluorescent LM for validation of the projection pathway in mid-sagittal CC slices. Further, the tissue preparation allowed regular LM for overview images and also TEM for axon diameter estimation.

5.5.1 Fluorescent LM - locating the transcallosal fibers of M1

The brains were manually sectioned into two hemisphere slabs (3-4 mm thick). The right hemisphere was sectioned sagittally into 40 µm-thick slices using a vibratome (VT1000s; Leica

Biosystems, Nussloch, DE) and placed on SuperFrost® slides (Menzel Gläser; ThermoScientific, Braunschweig, DE), mounted with Fluoroshield (w/ DAPI, #F6057, SigmaAldrich), and covered with Coverslips (size #0, Menzel Gläser).

A "super image" was obtained using a series of 10x magnification images, which were automatically stitched together by "Stereology" (Visiopharm; Hørsholm, Denmark) microscopy software (see Fig. 2b). Inspection of the sagittal slice revealed enhanced yellow fluorescent protein (EYFP) expression in the dorsal-anterior midbody of CC and informed the subsequent puncture procedure.

5.5.2 Histological preparation for LM and TEM

Having visualized where the axons from the excitatory neurons in M1 projected through CC, we prepared the same brains for LM and TEM for quantification of axon diameters and myelin thickness.

5.5.2.1 Epon embedding of fixed tissue

To determine the axon diameter distribution histologically within the same brains, the midsagittal slab from the left hemisphere was punctured using a biopsy puncture tool Ø = 1 mm (EMSdiasum, AxLab, Denmark) covering the region corresponding to the locus where virally transfected neurons are projecting through CC. To maintain correct orientation in the axonal projection direction, the samples were embedded in 2% Agar. The Agar-embedded puncture samples were transferred to a 2.5% solution of glutaraldehyde in cacodylate buffer (0.1 M) and stored for two weeks. Thereafter, Epon embedding was conducted following a standard procedure [18]. The samples were washed for 4 x 15 min in 0.1M cacodylate buffer, stained for two hours in a 2% OsO_4 in 0.1 M cacodylate buffer, and then washed for 2 x 30 min in 0.1 M cacodylate buffer,. The samples were then placed in fresh 0.1 M cacodylate buffer for overnight storage at 4 °C. The following day, the samples were dehydrated in a series of increasing alcohol solutions [30, 50, 70, 80, 90]% for 30 minutes each, and finally in 100% ethanol for 2 x 40 minutes. To remove residual ethanol, the dehydration was followed by submersion in propylene oxide for 3 x 10 min. Two solutions ("A" and "B") of Epon-812 (45345, Merck) were made with different hardeners, DDSA (45346, Merck) and MNA (45347, Merck), respectively. Solution A had a w/w ratio of 47:64 and solution B a 60:50 ratio. One hour before infiltration, the two solutions were mixed in a 1:1 ratio and 7 drops of accelerator DMP-30 (45348, Merck) per 10 mL of Epon-mixture was added. The infiltration was performed with increasing Epon concentrations in Epon:Propylene Oxide mixtures [1:1 for 1 hour, 2:1 for 1 hour] and finally in pure Epon mixture overnight at 4 °C. The following day, the samples were transferred to a new pure Epon mixture and polymerized in a heating chamber (N6c, Genlab; Widnes, England) for 48 hours at 60 ºC.

5.5.2.2 Cryofixation of fresh tissue

As the classical Epon-embedding is known to cause tissue shrinkage [17,19,28,33], we also performed cryo-embedding of CC samples of fresh tissue of a similar animal neither being MRI scanned nor being exposed to the optogenetic stimulation experiment. One (rat4.2) young adult (58 days old) Sprague-Dawley male rat (NTac:SD-M) was perfusion fixed with minor adjustments from the method described above. To minimize the degree of fixation, the transcardial perfusion with 4% formaldehyde was carried out for only 3 minutes at 15 mL/min. Thereafter, the brain was carefully extracted and a sagittal slab covering the midbrain was cut using a matrix (brain matrix, EMS diasum). We then obtained 200 µm-thick slices of the slab with a Vibratome (VT1000s; Leica Biosystems, Nussloch, DE). A biopsy puncture from the central

midbody of the CC was extracted with a biopsy puncture tool (EMSdiasum, AxLab, Denmark) Following 2 hours of storage in KPBS, the puncture sample was placed in an aluminum specimen carrier (Ø = 3 mm; Leica Microsystems, Wetzlar, Germany) and underwent freezing in a high-pressure freezer (HPM100; Leica Microsystems, Wetzlar, Germany). This was immediately followed by freeze substitution (AFS2; Leica Microsystems, Wetzlar, Germany) using 1% OsO_4 in acetone, which allowed for consecutive Epon infiltration and embedding of the sample. Ultrathin sections (50-70 nm) were made with the ultra-microtome (EM UC7; Leica Microsystems, Wetzlar, Germany) and collected on copper grids. Contrast enhancement was performed using a double staining protocol with uranyl acetate and lead citrate solutions (EM AC20; Leica Microsystems, Wetzlar, Germany).

5.5.2.3 Sectioning for LM and TEM

After embedding in Epon, we made a coarse trimming of the blocks using manually cut (7800 Knifemaker, LKB; Bromma, Sweden) glass knives (Ultra Glass Knife Strips #71014, EMS; Washington, PA, USA) on an ultramicrotome (Ultracut UCT or EM UC7; Leica Microsystems, Wetzlar, Germany). For LM, 1 µm-thick sections were cut with an 8.0 mm diamond knife (Diatome Histo AT 110, 8.0 mm; Nidau, Switzerland), mounted on microscopy slides (SuperFrost®Plus, 25x75x1 mm; ThermoScientific, Menzel-Gläser, Braunschweig, Germany), and set to dry at 50 °C on a heatbed (Medite OTS 40; Burgdorf, Germany). The mounted slides were then exposed to specific histological staining of myelin sheets with p-phenylenediamine (PPD; 1% w/v in a 50:50 solution of methanol:isopropanol) for 3 min, and briefly washed in acetone.

To measure axon diameters and myelin from TEM, we obtained ultra-thin sections (~ 40-70 nm) from the Epon-embedded samples using an ultramicrotome (Ultracut UCT or EM UC7, Leica Microsystems, Wetzlar, Germany). The sections were mounted on copper slot grids with a FORMVAR membrane. To obtain proper contrast to myelin for TEM, the sections are automatically stained on the grids with uranyl acetate and lead citrate (EM AC20; Leica Microsystems, Wetzlar, Germany).

5.5.3 Microscopy and image segmentation

5.5.3.1 LM of Epon-embedded samples

We initially obtained overview images (2752 x 2192 px, Lumenera; MBF Bioscience, Williston, VT, USA) of the Ø = 1 mm samples on LM (Olympus BX 60; Olympus Europe, Hamburg, DE) with a 10x lens (NA: 0.30; UPlanFI; Olympus).

5.5.3.2 TEM of Epon-embedded samples

TEM images were obtained on a CM100 microscope (Philips; FEI, Eindhoven, NL). The CC sample, approximately encompassing the M1 axon tracts, was imaged at 4200x magnification in a sequential manner to cover the entire CC cross section in the Ø=1mm punctured sample. This resulted in images (2048 x 2048 pixels per image; 12 nm/pixel; ~24.6 x 24.6 µm) numbering from 16 from the top part of CC (N=1) to 69-77 images (N=4), which were acquired in an unbiased manner throughout the sample. We took care to avoid overlap of the images, any such regions from the first animal (N=1) were manually discarded from the stitched super image ("Stitching Tool" [84] in FIJI) to avoid overcounting of the same axons. The segmentation of

the acquired images was obtained using AxonDeepSeg [46], using the built-in pre-trained model for TEM images. The model provided individual inner (d) axon diameters based on the segmented area and assuming the circular cross sections, as well as the corresponding g-ratios of all segmented axons. The acquired axon diameter distributions were filtered between 0.25 and 5.0 µm, based on visual inspection.

5.5.3.3 TEM of Cryo-fixed tissue samples

TEM images of the cryo-fixed and Epon-embedded samples were obtained using the same microscope as above (CM100, Philips; FEI, Eindhoven, NL), with a pixel size of 8.55 nm and field of view (FOV) spanning 2048 x 2048 pixels, thus corresponding to approximately 17.5 x 17.5 µm. Fifteen TEM images were obtained from different positions within the same section and were then aligned relative to each other on a lower magnification image. The automatic segmentation method did not immediately work for cryo-TEM images due to their differing image contrast. Therefore, we manually segmented 607 axons in ITK Snap (RRID:SCR_002010) using the polygon tool and the adaptive paintbrush tool. The intra-axonal space was here defined as the area bounded by the innermost myelin layer. A connected components analysis of the segmented axons was then performed in MATLAB 2020a. Owing to the eccentricity of many of the axonal cross sections, the minor axis of an ellipse was used to represent axon diameter. The obtained axon diameter distributions were filtered between 0.1 µm and 5.0 µm, resulting in 603 axons. This lower diameter detection was feasible for the highly detailed cryo-TEM images, which allowed measurement of myelinated axons below 0.25 µm diameter in contrast to the Epon-TEM images

5.6 Calculating the structure-function relationship between conduction velocity and axon diameter

From the obtained length of the projection pathway (L) and the measured TCT, we calculated the estimated conduction velocity (CV) as follows:

$$\mathbf{CV = L / TCT} \qquad \mathbf{(1)}$$

Similarly, we calculated the conduction velocity along the pathways from the measured g-ratio and axon diameter, given Hursh's structure-function relationship [1,5,10]:

$$\mathbf{CV = (5.5/g) * d} \qquad \mathbf{(2)}$$

where g, i.e., the g-ratio, was set to group mean of EM data results, rather than the literature value of ~0.7 [10,20,33] Hence, combining Eq. (1) and (2) allows us to predict the TCT from structural measures, or the converse prediction of axon diameter from the functional measure.

5.7 Statistical analysis

5.7.1 Opto-ElPhys

Signal data from the two channels of the stereotrodes were averaged for each trial. For peak detection, all 150 trials for each condition were averaged. The coefficient of variation was calculated as the standard deviation (SD) of the signal amplitude of all individual trials at the exact sample of the peak latency, divided by the mean signal amplitude at the peak latency. A condition was considered reliable when the coefficient of variation of the trials was less than 1.00. Median latencies of all robust conditions were used to represent the latency of each animal,

presented in violin plots (Fig. 1b). Medians of all animals along with whisker plots of most extreme values are indicated with vertical lines.

5.7.2 Axon diameter distributions from histology

To quantify the axon diameter distributions of the measured diameters from histology, we fitted gamma distributions with parameters *a* (shape), and *b* (scale), and used a location parameter of 0. Statistical features were expressed as the mean, SD, and the mode. The voxel-wise dMRI diameter estimates are weighted towards larger diameters, in part due to their larger volumes [27,41] and in part due to the nature of the scaling of the signal attenuation with diameter [36,42,43]. As such, the arithmetic means of the histological axon diameter distribution will not match the diameter index measured with dMRI. We accounted for this weighting by calculating the weighted diameter (d_w) from the histological axon diameter distributions. The weighting depends on the dMRI protocol used and upon the axon diameter distribution. In the wide pulse limit, $\delta \gg R^2/D_0$ [36,42,43], where R is the axon radius from histology, D_0 is the intrinsic diffusivity and δ is the pulse-width of the diffusion encoding. In practice, this wide-pulse limit applies to most axons in the rat brain [34] Using this assumption we can calculate d_w as [36,42]:

$$\boldsymbol{d_w = 2\left(\frac{<R^6>}{<R^2>}\right)^{0.25}} \qquad \textbf{(Eq. 3)}$$

6. Conflicts of Interest

GC Europe generously provided CSS with dental acrylic cement, mixing apparatus, and application tools. HRS has received honoraria as speaker and consultant from Lundbeck Pharma A/S, Denmark, and as editor in chief (Neuroimage Clinical) from Elsevier Publishers, Amsterdam, The Netherlands. HRS has received royalties as a book editor from Springer Publishers, Stuttgart, Germany and Gyldendal Publishers, Copenhagen, Denmark, Oxford University Press, Oxford, UK.

7. Funding

CSS and MA were supported by the Capital Region Research Foundation Grant (grant number A5657; Principal investigator: TBD). CSS was supported by Lundbeck Foundation travel stipend (R315-2019-915). MP was supported by funding from the European Union's Horizon 2020 research and innovation programme under the Marie Skłodowska-Curie grant agreement No 754462. HRS holds a 5-year professorship in precision medicine at the Faculty of Health Sciences and Medicine, University of Copenhagen, which was sponsored by the Lundbeck Foundation from 2017-2022 (grant number R186-2015-2138). The project has received funding from the European Research Council (ERC) under the European Union's Horizon Europe research and innovation programme (grant agreement No. 101044180; Principal investigator: TBD).

8. Acknowledgements

Thanks to local Laboratory Technician, Sascha Gude, for her immense help with animal caretaking and assisting in experiments, throughout the project period. Thanks to laboratory technician Susanne Sørensen from Bispebjerg Hospital for her help with sample preparation for both light and electron microscopy. Thanks to H. Martin Kjer for aiding in initial axon segmentation methods for LM data - and ideas for visualization. Last, but certainly not least, thanks

to the late Bente Pakkenberg for her invaluable inputs and guidance during laboratory experiments and manuscript revision – initially as a co-author. The present study builds upon her pioneering work on corpus callosum and she will be sincerely missed as a person - and researcher.

9. References

1. Hursh, J. B. Conduction velocity and diameter of nerve fibers. *Am J Physiol* **127**, 131–139 (1939).
2. Rushton, W. A. H. A theory of the effects of fibre size in medullated nerve. *The Journal of physiology* **115**, 101–122 (1951).
3. Sanders, F. K. & Whitteridge, D. Conduction velocity and myelin thickness in regenerating nerve fibres. *The Journal of physiology* **105**, 152–174 (1946).
4. Smith, R. S. & Koles, Z. J. Myelinated nerve fibers: computed effect of myelin thickness on conduction velocity. *The American journal of physiology* **219**, 1256–1258 (1970).
5. Waxman, S. G. & Bennett, M. V. Relative conduction velocities of small myelinated and non-myelinated fibres in the central nervous system. *Nature: New biology* **238**, 217–219 (1972).
6. Waxman, S. G. & Swadlow, H. A. Ultrastructure of visual callosal axons in the rabbit. *Experimental neurology* **53**, 115–127 (1976).
7. Innocenti, G. M., Vercelli, A. & Caminiti, R. The diameter of cortical axons depends both on the area of origin and target. *Cerebral cortex (New York, N.Y. : 1991)* **24**, 2178–2188 (2014).
8. Stikov, N. *et al.* Quantitative analysis of the myelin g -ratio from electron microscopy images of the macaque corpus callosum. *Data in Brief* **4**, 368–373 (2015).
9. Chomiak, T. & Hu, B. What is the optimal value of the g-ratio for myelinated fibers in the rat CNS? A theoretical approach. *PloS one* **4**, e7754 (2009).
10. Tettoni, L., Lehmann, P., Houzel, J. C. & Innocenti, G. M. Maxsim, software for the analysis of multiple axonal arbors and their simulated activation. *Journal of neuroscience methods* **67**, 1–9 (1996).
11. Arancibia-Cárcamo, I. L. *et al.* Node of Ranvier length as a potential regulator of myelinated axon conduction speed. *eLife* **6**, (2017).
12. Drakesmith, M. *et al.* Estimating axon conduction velocity in vivo from microstructural MRI. *NeuroImage* **203**, 116186 (2019).
13. Aboitiz, F., Morales, D. & Montiel, J. The evolutionary origin of the mammalian isocortex: towards an integrated developmental and functional approach. *The Behavioral and brain sciences* **26**, 535–52; discussion 552-85 (2003).
14. Assaf, Y., Bouznach, A., Zomet, O., Marom, A. & Yovel, Y. Conservation of brain connectivity and wiring across the mammalian class. **23**, 805–808 (2020).
15. Owen, R. On the structure of the brain in marsupial animals. *Phil. Trans. R. Soc* **127**, 87–96 (1837).
16. Aboitiz, F., Scheibel, A. B., Fisher, R. S. & Zaidel, E. Fiber composition of the human corpus callosum. *Brain research* **598**, 143–153 (1992).
17. Caminiti, R., Ghaziri, H., Galuske, R., Hof, P. R. & Innocenti, G. M. Evolution amplified processing with temporally dispersed slow neuronal connectivity in primates. *Proceedings of the National Academy of Sciences of the United States of America* **106**, 19551–19556 (2009).
18. Riise, J. & Pakkenberg, B. Stereological estimation of the total number of myelinated callosal fibers in human subjects. *Journal of anatomy* **218**, 277–284 (2011).
19. Tomasi, S., Caminiti, R. & Innocenti, G. M. Areal differences in diameter and length of corticofugal projections. *Cerebral cortex (New York, N.Y. : 1991)* **22**, 1463–1472 (2012).
20. Caminiti, R. *et al.* Diameter, length, speed, and conduction delay of callosal axons in macaque monkeys and humans: comparing data from histology and magnetic resonance imaging diffusion tractography. *The Journal of neuroscience : the official journal of the Society for Neuroscience* **33**, 14501–14511 (2013).
21. Swadlow, H. A., Rosene, D. L. & Waxman, S. G. Characteristics of interhemispheric impulse conduction between prelunate gyri of the rhesus monkey. *Experimental brain research* **33**, 455–467 (1978).
22. Ferbert, A. *et al.* Interhemispheric inhibition of the human motor cortex. *The Journal of physiology* **453**, 525–546 (1992).
23. Di Lazzaro, V. *et al.* Direct demonstration of interhemispheric inhibition of the human motor cortex produced by transcranial magnetic stimulation. *Exp Brain Res* **124**, 520–524 (1999).
24. Mochizuki, H., Huang, Y.-Z. & Rothwell, J. C. Interhemispheric interaction between human dorsal premotor and contralateral primary motor cortex. *J Physiol* **561**, 331–338 (2004).
25. Rogasch, N. C., Daskalakis, Z. J. & Fitzgerald, P. B. Cortical inhibition, excitation, and connectivity in schizophrenia: a review of insights from transcranial magnetic stimulation. *Schizophrenia bulletin* **40**, 685–696 (2014).
26. Ni, Z. *et al.* Measuring latency distribution of transcallosal fibers using transcranial magnetic stimulation. *Brain Stimul* **13**, 1453–1460 (2020).
27. Alexander, D. C. *et al.* Orientationally invariant indices of axon diameter and density from diffusion MRI. *NeuroImage* **52**, 1374–1389 (2010).
28. Dyrby, T. B., Innocenti, G. M., Bech, M. & Lundell, H. Validation strategies for the interpretation of microstructure imaging using diffusion MRI. *Neuroimage* **182**, 62–79 (2018).

29. Barazany, D., Basser, P. J. & Assaf, Y. In vivo measurement of axon diameter distribution in the corpus callosum of rat brain. *Brain : a journal of neurology* **132**, 1210–1220 (2009).
30. Horowitz, A. *et al.* In vivo correlation between axon diameter and conduction velocity in the human brain. *Brain structure & function* **220**, 1777–1788 (2015).
31. Lee, H.-H. *et al.* Along-axon diameter variation and axonal orientation dispersion revealed with 3D electron microscopy: implications for quantifying brain white matter microstructure with histology and diffusion MRI. *Brain Struct Funct* **224**, 1469–1488 (2019).
32. Abdollahzadeh, A., Belevich, I., Jokitalo, E., Tohka, J. & Sierra, A. Automated 3D Axonal Morphometry of White Matter. *Sci Rep* **9**, 6084 (2019).
33. Andersson, M. *et al.* Axon morphology is modulated by the local environment and impacts the noninvasive investigation of its structure-function relationship. *Proc Natl Acad Sci U S A* **117**, 33649–33659 (2020).
34. Andersson, M. *et al.* Does powder averaging remove dispersion bias in diffusion MRI diameter estimates within real 3D axonal architectures? *NeuroImage* **248**, 118718 (2022).
35. Fan, Q. *et al.* Axon diameter index estimation independent of fiber orientation distribution using high-gradient diffusion MRI. *NeuroImage* **222**, 117197 (2020).
36. Veraart, J. *et al.* Nonivasive quantification of axon radii using diffusion MRI. *eLife* **9**, (2020).
37. Veraart, J., Raven, E. P., Edwards, L. J., Weiskopf, N. & Jones, D. K. The variability of MR axon radii estimates in the human white matter. *Hum Brain Mapp* **42**, 2201–2213 (2021).
38. Dyrby, T. B., Sogaard, L. V., Hall, M. G., & others. Contrast and stability of the axon diameter index from microstructure imaging with diffusion MRI. *Magn Reson Med* **70**, 711–721 (2013).
39. Sepehrband, F., Alexander, D. C., Kurniawan, N. D., Reutens, D. C. & Yang, Z. Towards higher sensitivity and stability of axon diameter estimation with diffusion-weighted MRI: Towards Higher Sensitivity and Stability of Axon Diameter Mapping. *NMR Biomed.* **29**, 293–308 (2016).
40. Nilsson, M., Lasič, S., Drobnjak, I., Topgaard, D. & Westin, C.-F. Resolution limit of cylinder diameter estimation by diffusion MRI: The impact of gradient waveform and orientation dispersion: Resolution limit of cylinder diameter estimation by diffusion MRI: the impact of gradient waveform and orientation dispersion. *NMR in Biomedicine* **30**, e3711 (2017).
41. Packer, K. J. & Rees, C. Pulsed NMR studies of restricted diffusion. I. Droplet size distributions in emulsions. *Journal of Colloid and Interface Science* **40**, 206–218 (1972).
42. Burcaw, L. M., Fieremans, E. & Novikov, D. S. Mesoscopic structure of neuronal tracts from time-dependent diffusion. *NeuroImage* **114**, 18–37 (2015).
43. Lee, H.-H., Jespersen, S. N., Fieremans, E. & Novikov, D. S. The impact of realistic axonal shape on axon diameter estimation using diffusion MRI. *NeuroImage* **223**, 117228 (2020).
44. Korogod, N., Petersen, C. C. H. & Knott, G. W. Ultrastructural analysis of adult mouse neocortex comparing aldehyde perfusion with cryo fixation. *eLife* **4**, (2015).
45. Skoven, C. S. *et al.* Dose-response relationship between the variables of unilateral optogenetic stimulation and transcallosal evoked responses in rat motor cortex. *Front. Neurosci.* **16**, 968839 (2022).
46. Zaimi, A. *et al.* AxonDeepSeg: automatic axon and myelin segmentation from microscopy data using convolutional neural networks. *Scientific reports* **8**, 3816 (2018).
47. Pesaresi, M. *et al.* Axon diameter and axonal transport: In vivo and in vitro effects of androgens. *NeuroImage* **115**, 191–201 (2015).
48. Tang-Wright, K. *et al.* Intra-Areal Visual Topography in Primate Brains Mapped with Probabilistic Tractography of Diffusion-Weighted Imaging. *Cerebral Cortex* **32**, 2555–2574 (2022).
49. Olivares, R., Montiel, J. & Aboitiz, F. Species differences and similarities in the fine structure of the mammalian corpus callosum. *Brain, behavior and evolution* **57**, 98–105 (2001).
50. Iordanova, B., Vazquez, A., Kozai, T. D., Fukuda, M. & Kim, S.-G. Optogenetic investigation of the variable neurovascular coupling along the interhemispheric circuits. *Journal of cerebral blood flow and metabolism : official journal of the International Society of Cerebral Blood Flow and Metabolism* **38**, 627–640 (2018).
51. Hoffmeyer, H. W., Enager, P., Thomsen, K. J. & Lauritzen, M. J. Nonlinear neurovascular coupling in rat sensory cortex by activation of transcallosal fibers. *Journal of cerebral blood flow and metabolism : official journal of the International Society of Cerebral Blood Flow and Metabolism* **27**, 575–587 (2007).
52. Seggie, J. & Berry, M. Ontogeny of interhemispheric evoked potentials in the rat: significance of myelination of the corpus callosum. *Exp Neurol* **35**, 215–232 (1972).
53. Perge, J. A., Niven, J. E., Mugnaini, E., Balasubramanian, V. & Sterling, P. Why do axons differ in caliber? *The Journal of neuroscience : the official journal of the Society for Neuroscience* **32**, 626–638 (2012).
54. McDougall, S. *et al.* Myelination of axons corresponds with faster transmission speed in the prefrontal cortex of developing male rats. *eNeuro* **5**, (2018).
55. Dyrby, T. B. *et al.* Interpolation of diffusion weighted imaging datasets. *NeuroImage* **103**, 202–213 (2014).

56. Dyrby, T. B. *et al.* An ex vivo imaging pipeline for producing high-quality and high-resolution diffusion-weighted imaging datasets. *Hum Brain Mapp* **32**, 544–563 (2011).
57. Peterchev, A. V., Goetz, S. M., Westin, G. G., Luber, B. & Lisanby, S. H. Pulse width dependence of motor threshold and input–output curve characterized with controllable pulse parameter transcranial magnetic stimulation. *Clinical Neurophysiology* **124**, 1364–1372 (2013).
58. Siebner, H. R. *et al.* Transcranial magnetic stimulation of the brain: What is stimulated? – A consensus and critical position paper. *Clinical Neurophysiology* **140**, 59–97 (2022).
59. Debanne, D., Campanac, E., Bialowas, A., Carlier, E. & Alcaraz, G. Axon physiology. *Physiological reviews* **91**, 555–602 (2011).
60. Costa, A. R., Pinto-Costa, R., Sousa, S. C. & Sousa, M. M. The Regulation of Axon Diameter: From Axonal Circumferential Contractility to Activity-Dependent Axon Swelling. *Front. Mol. Neurosci.* **11**, 319 (2018).
61. Houzel, J. C., Milleret, C. & Innocenti, G. Morphology of callosal axons interconnecting areas 17 and 18 of the cat. *The European journal of neuroscience* **6**, 898–917 (1994).
62. Töpperwien, M., Markus, A., Alves, F. & Salditt, T. Contrast enhancement for visualizing neuronal cytoarchitecture by propagation-based x-ray phase-contrast tomography. *NeuroImage* **199**, 70–80 (2019).
63. Lamantia, A.-S. & Rakic, P. Cytological and quantitative characteristics of four cerebral commissures in the rhesus monkey. *J. Comp. Neurol.* **291**, 520–537 (1990).
64. Pizzolato, M., Canales-Rodríguez, E. J., Andersson, M. & Dyrby, T. B. Axial and radial axonal diffusivities and radii from single encoding strongly diffusion-weighted MRI. *Medical Image Analysis* **86**, 102767 (2023).
65. Fan, Q. *et al.* Scan-rescan repeatability of axonal imaging metrics using high-gradient diffusion MRI and statistical implications for study design. *NeuroImage* **240**, 118323 (2021).
66. Aravanis, A. M. *et al.* An optical neural interface: in vivo control of rodent motor cortex with integrated fiberoptic and optogenetic technology. *J Neural Eng* **4**, S143–S156 (2007).
67. Jiang, X. *et al.* Principles of connectivity among morphologically defined cell types in adult neocortex. *Science* **350**, aac9462 (2015).
68. Barth, A. L. *et al.* Comment on "Principles of connectivity among morphologically defined cell types in adult neocortex". *Science* **353**, 1108–1108 (2016).
69. Rock, C., Zurita, H., Lebby, S., Wilson, C. J. & Apicella, A. J. Cortical Circuits of Callosal GABAergic Neurons. *Cereb Cortex* **28**, 1154–1167 (2018).
70. Kumar, S. S. & Huguenard, J. R. Properties of Excitatory Synaptic Connections Mediated by the Corpus Callosum in the Developing Rat Neocortex. *Journal of Neurophysiology* **86**, 2973–2985 (2001).
71. Palmer, L. M. *et al.* The cellular basis of GABA(B)-mediated interhemispheric inhibition. *Science* **335**, 989–993 (2012).
72. Palmer, L. M., Schulz, J. M. & Larkum, M. E. Layer-specific regulation of cortical neurons by interhemispheric inhibition. *Commun Integr Biol* **6**, e23545 (2013).
73. Makarov, V. A., Schmidt, K. E., Castellanos, N. P., Lopez-Aguado, L. & Innocenti, G. M. Stimulus-dependent interaction between the visual areas 17 and 18 of the 2 hemispheres of the ferret (Mustela putorius). *Cereb Cortex* **18**, 1951–1960 (2008).
74. Kaur, S., Lazar, R. & Metherate, R. Intracortical pathways determine breadth of subthreshold frequency receptive fields in primary auditory cortex. *J Neurophysiol* **91**, 2551–2567 (2004).
75. Bak & Nielsen. REPULSION, A novel approach to efficient powder averaging in solid-state NMR. *Journal of magnetic resonance (San Diego, Calif. : 1997)* **125**, 132–139 (1997).
76. Jones, D. K., Horsfield, M. A. & Simmons, A. Optimal strategies for measuring diffusion in anisotropic systems by magnetic resonance imaging. *Magnetic resonance in medicine* **42**, 515–525 (1999).
77. P. A. Cook, Y. Bai, S. N.-G., K. K. Seunarine, M. G. Hall, G. J. Parker, D. C. Alexander. Camino: Open-source diffusion-MRI reconstruction and processing. in *Proc. Intl. Soc. Mag. Reson. Med.* vol. 14 2759 (2006).
78. Ma, X., Uğurbil, K. & Wu, X. Denoise magnitude diffusion magnetic resonance images via variance-stabilizing transformation and optimal singular-value manipulation. *NeuroImage* **215**, 116852 (2020).
79. Kellner, E., Dhital, B., Kiselev, V. G. & Reisert, M. Gibbs-ringing artifact removal based on local subvoxel-shifts. *Magnetic resonance in medicine* **76**, 1574–1581 (2016).
80. McKinnon, E. T., Helpern, J. A. & Jensen, J. H. Modeling white matter microstructure with fiber ball imaging. *NeuroImage* **176**, 11–21 (2018).
81. Kroenke, C. D., Ackerman, J. J. H. & Yablonskiy, D. A. On the nature of the NAA diffusion attenuated MR signal in the central nervous system. *Magn. Reson. Med.* **52**, 1052–1059 (2004).
82. Kaden, E., Kruggel, F. & Alexander, D. C. Quantitative mapping of the per-axon diffusion coefficients in brain white matter: Quantitative Mapping of the Per-Axon Diffusion Coefficients. *Magn. Reson. Med.* **75**, 1752–1763 (2016).

83. van Gelderen, P., Despres, D., Vanzijl, P. C. M. & Moonen, C. T. W. Evaluation of Restricted Diffusion in Cylinders. Phosphocreatine in Rabbit Leg Muscle. *Journal of Magnetic Resonance, Series B* **103**, 255–260 (1994).
84. Preibisch, S., Saalfeld, S. & Tomancak, P. Globally optimal stitching of tiled 3D microscopic image acquisitions. *Bioinformatics (Oxford, England)* **25**, 1463–1465 (2009).